Materials and Design 195 (2020) 108971

Contents lists available at ScienceDirect

Materials and Design

journal homepage: www.elsevier.com/locate/matdes

Understanding elastic anisotropy in diamond based lattice structures produced by laser powder bed fusion: Effect of manufacturing deviations

Markel Alaña [a,1,*], Antonio Cutolo [b,1,*], Gabriel Probst [b], Sergio Ruiz de Galarreta [a], Brecht Van Hooreweder [b,c]

[a] Department of Mechanical Engineering and Materials, Universidad de Navarra, TECNUN Escuela de Ingenieros, Paseo Manuel de Lardizabal, 13, 20018 San Sebastian, Spain
[b] KU Leuven Department of Mechanical Engineering, Celestijnenlaan 300, 3001 Leuven, Heverlee, Belgium
[c] Members Flanders Make, Leuven, Belgium

HIGHLIGHTS

- Manufacturing imperfections are aligned with the building direction and thus affect the anisotropy of the lattice structures.
- Probability distributions of the imperfections were obtained depending on the position of the cross-sections along the strut.
- The FE model with imperfections predicts the stiffest direction to change from [111] to [110] as reported in literature.
- The offset of the center of gravity of the strut cross section had the greatest effect in the anisotropy variation.

GRAPHICAL ABSTRACT

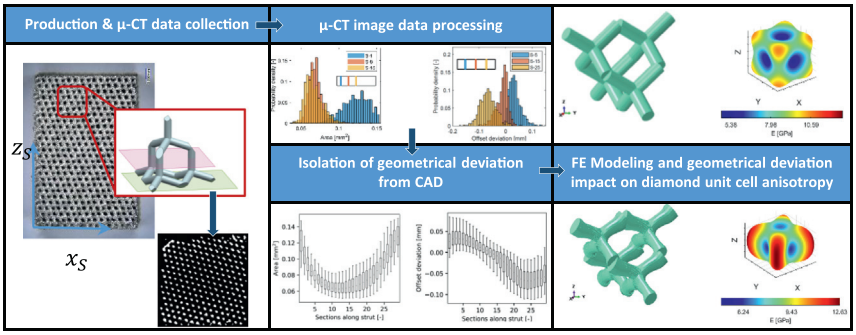

ARTICLE INFO

Article history:
Received 28 May 2020
Received in revised form 2 July 2020
Accepted 9 July 2020
Available online 16 July 2020

Keywords:
Laser powder bed fusion - Ti-6Al-4 V - lattice structures - anisotropy - FE modeling

ABSTRACT

Laser powder bed fusion (L-PBF) allows the production of metal lattice cellular structures with tailored mechanical properties. In order to generate the specific structural behavior it is of utmost importance to understand the response of the unit cells when different load conditions are considered. In this article the mechanical response of diamond based cellular structures has been investigated focusing on the impact of geometrical inaccuracy generated by the manufacturing process on the elastic anisotropy of the mentioned unit cell. The μ-CT analysis of the structures shows that the manufacturing deviations occur in certain orientations that depend highly on the building direction and proximity to nodes. The measured imperfection types were implemented in a finite element model in order to predict their single and combined effects in the elastic directional response. The results indicate that the L-PBF process can induce a significant change of elastic anisotropy in the diamond unit cells, including a substantial variation of the optimal orientation for minimal compliance. Methods are presented to calculate this anisotropy such that it can be taken into account when designing and using such lattice structures in real-life applications with multi-axial load conditions.

1. Introduction

Metal additive manufacturing (AM) refers to the production of metallic components in a layer by layer fashion from a specific computer-aided design (CAD) model. Among the AM processes the laser powder bed fusion (L-PBF) process uses a focused and computer controlled

* Corresponding authors.
E-mail addresses: malana@tecnun.es (M. Alaña), antonio.cutolo@kuleuven.be (A. Cutolo).
[1]Contributed equally to this work.

https://doi.org/10.1016/j.matdes.2020.108971

laser beam to selectively melt metal powder. This technique offers an attractive method for producing complex near net-shape geometries with an efficient material use [1]. One of the big advantages of using this AM technique is the possibility to produce parts with almost unlimited freedom in terms of geometrical design. This allows the integration of lattice structures in the design phase to target specific mechanical properties in designated locations while reducing the total weight of the component. Apart from their load bearing applications, lattice structures are also used in other fields for energy absorption, heat transfer devices, vibration attenuation or as cellular catalysts, among others [2–4].

Lattice structures are defined in this work as a class of cellular solids formed by beam like members named struts that connect nodes [5–7]. The struts are arranged in a fixed topology to generate the unit cell (UC) that is replicated in the 3D space to fill the volume of the structure.

According to Maxwell's stability criterion, UCs can be classified in stretching dominated and in bending dominated structures [8]. This paper will focus on the diamond unit cell, which is a bending dominated structure. The mechanical properties of lattice structures depend on several factors: (i) the type, size and topology of the UC; (ii) the relative density of the lattice structure defined as the quantity of material in the volume of the lattice structure; (iii) the parent material used for the production; and (iv) the material porosity and surface quality. Moreover, during recent years, in order to better integrate cellular lattice structures in load bearing applications, several authors have introduced the importance of understanding the UC elastic anisotropy behavior and the effect of load directions on static and dynamic properties of lattice structures [9–13].

In addition, some inherent geometrical imperfections may occur during the manufacturing process leading to deviations from the ideal structure. This phenomena can be more pronounced when the struts dimensions (length and/or diameter) approach the laser spot diameter [14]. Therefore it is essential to evaluate the impact of these geometrical imperfections on the structural response of the final component.

Several authors investigated the impact of geometrical imperfection on mechanical properties of metal lattice structures [15–17]. Dallago et al. [18] used micro X-ray computer tomography to measure and classify the types of morphological imperfections in terms of deviation from the CAD model of regular cubic Ti6Al4V cellular lattices. The authors highlighted that struts with a small angle with respect to the building platform are systematically affected by dross formation that increases the struts thickness and offsets the center of gravity of the cross-sections from the imaginary axis that connects the two nodes introducing a sort of “waviness”. The data gathered from $\mu - CT$ were used to build different FE models with increasing level of complexity. From these simulations, Dallago et al. concluded that the higher thickness of the as-produced struts increased the overall stiffness of the cellular structure while the bending actions introduced by the waviness reduced the elastic stiffness. A comparable study with similar conclusions was made by Lei et al. [19] in which X-ray micro-computed tomography ($\mu - CT$) was employed to extract the geometrical deviations and to quantify the statistical distribution of strut diameter of two different unit cells, i.e. the BCC and the BCCZ produced with AlSi10Mg. The reconstructed models were used to analyze the impact of the distribution of the imperfections on the structure's response. Lozanovski et al. [20] followed a similar procedure to design very detailed geometrical models that included shape variation and “waviness” obtained from $\mu - CT$ scans.

On the other hand, Liu [21] and Xiao [22] simulated the mechanical properties of octet truss, rhombic dodecahedron and ideal rhombicuboctahedron along different directions, accounting for manufacturing deviations with respect to the ideal geometry. Liu and Xiao concluded that the manufacturing induced deviations had an important effect on the anisotropy of the studied lattices structures. Nevertheless, tests were performed with a fixed orientation between the load and the unit cell.

Wauthle et al. [9] were among the first researchers to investigate the elastic anisotropy of the cubic diamond UC produced with L-PBF in Ti6Al4V. However, due to the high level of internal defects generated during the manufacturing process i.e. pores and lack of fusion defects, the authors were not able to conclude on the effective anisotropic behavior of the diamond UC. Cutolo et al. [11] investigated the same topic highlighting a high level of elastic anisotropy of the diamond UC by testing the same lattice structure along different load directions. However, none of the above-mentioned studies included an investigation on the effect of the different morphological imperfections on the anisotropic behavior of the lattice structure.

The objective of the present study is to understand both the individual and combined impact of the different types of geometrical deviations on the elastic anisotropy response of Ti6Al4V diamond UC produced by L-PBF. In order to do so, a detailed analysis of the inherent geometrical imperfections was carried out. The morphology of the as produced lattice structures was reconstructed via $\mu - CT$ and different manufacturing imperfection types were classified in terms of deviation from the CAD model. The novelty of this research is that the deviation types were analyzed by considering their statistical distribution along the strut axis. From statistical analysis of $\mu - CT$ data, different beam FE models were created, with different levels of complexity to isolate the impact of the different types of geometrical deviations on the anisotropy of the diamond unit cells.

An overview of the methodology used to generate the different FE models is presented in Fig. 1. Experimental results obtained by Cutolo et al. that were reported in [11] show that the produced diamond based lattice structures have different anisotropy behavior with respect to the idealized UC model. The numerical results of this study are in line with the previous work by Cutolo et al., and indicate that the variation in the anisotropic response can be mainly attributed to the offset of the center of gravity of the struts cross-sections with respect to the ideal strut axis.

2. Materials and methods

2.1. Manufacturing

The samples considered in this investigation have been described in the recent work from Cutolo et al. [11] in which a diamond unit cell has been used for the creation of Ti6Al4V lattice structures to investigate the effect of load direction on the mechanical properties of diamond based cellular structures. A diamond unit cell can be described as an assembly of struts and nodes with an angle of 109.48 deg between each pair of struts connecting one node. From a manufacturing point of view, the main advantage of using this unit cell is that the strut angles with the build platform of the L-PBF machine is always 35.26 deg. This angle is high enough to guarantee a production of these struts via L-PBF without using support structures.

The studied samples were prisms with a square cross-section and with a side D of $10mm$ and height H of $15mm$. A unit cell size of $1mm$ was used with a prescribed relative density of 25%. The authors divided the samples in three batches according to the orientation between the load direction and UC orientation, i.e. [001], [111] and [011] as shown in Fig. 2. The orientation of all the diamond unit cells (X_U, Y_U, Z_U) with respect to the L-PBF base plate (X_L, Y_L) was chosen constant and equal for all samples, such that indeed all unit cell struts of all samples were at the same angle of 35.26 with respect to this base plate (X_L, Y_L). This guarantees equal unit cell quality and morphology for all samples. The orientation of the samples surrounding all unit cells (i.e. the lattice structures, X_S, Y_S, Z_S) with respect to the L-PBF base plate (X_L, Y_L) was varied as indicated in Fig. 2 to enable different load directions with respect to the unit cell orientation, and the obtained manufactured samples are shown in Fig. 3. A detailed description of sample design, production and testing is reported in [11].

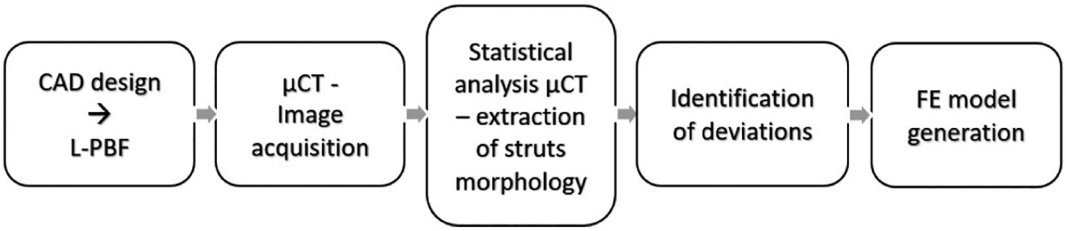

Fig. 1. Procedure for generating FE models.

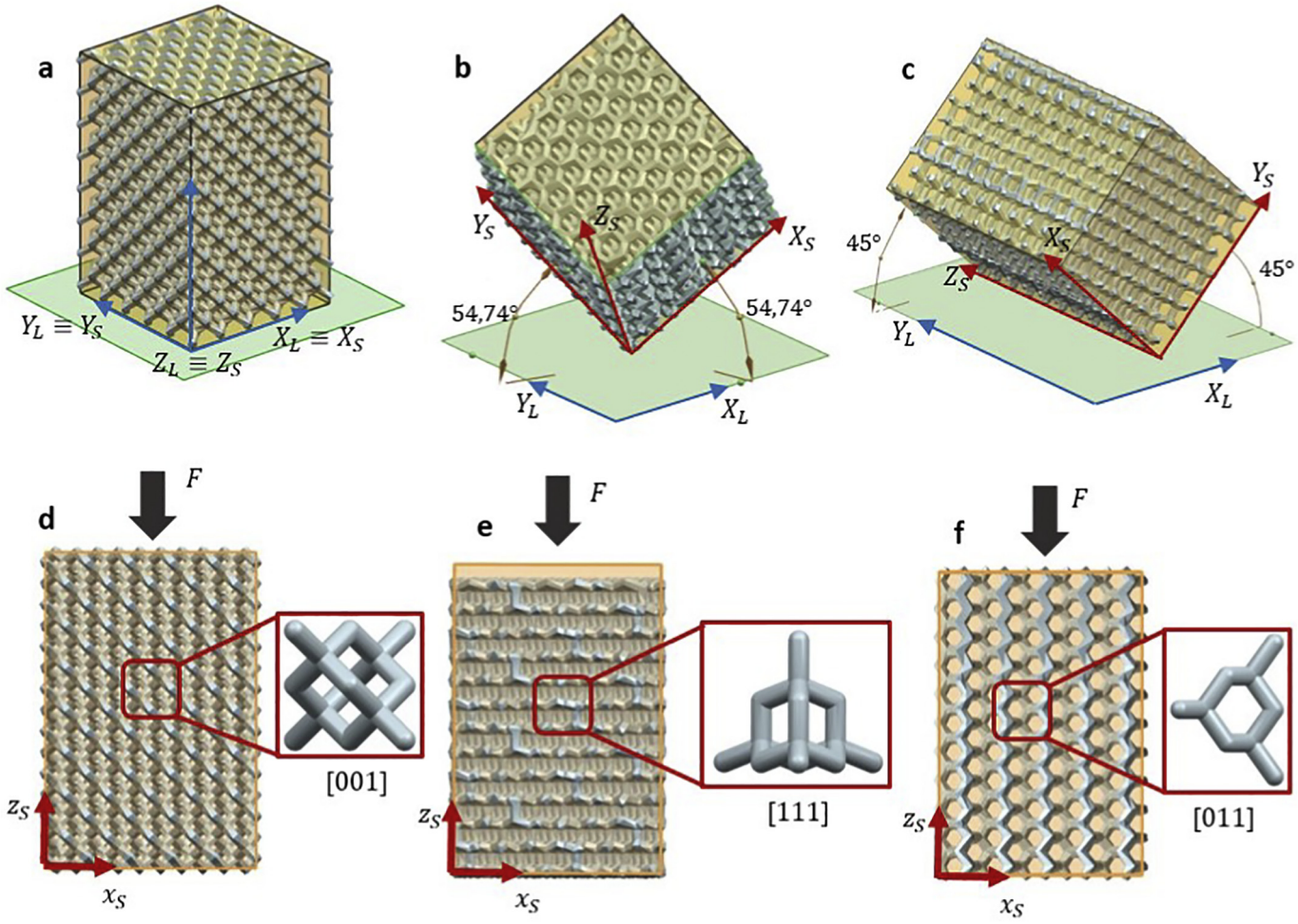

Fig. 2. Samples orientation with respect to the build platform X_L, Y_L for a) [001], b) [111], c)[011] orientation Force direction with respect to the UC for d) [001], e) [111], f) [011] orientation [11].

2.2. Analysis of manufactured structures

From each batch, two samples were analyzed with a Nikon XT H225 ST CT-system to evaluate the morphological differences between the CAD geometry and the produced samples. A *W* target and 1*mm* Cu filter were used during the scanning and the machine was set to a voltage of $[135 - 165]kV$ and a current of $[5070]\mu A$. The voxel size was $12\mu m$. $\mu - CT$ data were exported in terms of stacked images parallel to the X_S, Y_S plane of the samples with a frequency of 84 images per millimeter along the Z_S direction.

The morphological information extraction was performed using $\mu - CT$ scan data from the [111] oriented specimens. In this case, the resulting stacked images are perpendicular to 4 struts per unit cell (Fig. 2-e). The topology of the diamond unit cell and the fixed orientation of the unit cell with respect to the L-PBF build-platform, ensure strut-to-strut homogeneity in terms of morphology for all the specimens and thus the same distribution of imperfections can be considered.

For every sliced image, ImageJ software was used to extract the area and the center of gravity of each strut cross-section, as well as the best ellipse fit with the dimensions and orientation of the major and minor axes with respect to the X_S and Y_S axes, as shown in Fig. 4. These data were processed with Matlab to isolate the morphology of every single strut by means of the following procedure:

- each strut was identified by the position of its center of gravity;
- a deviation tolerance from the center of gravity was used to create a region of interest;

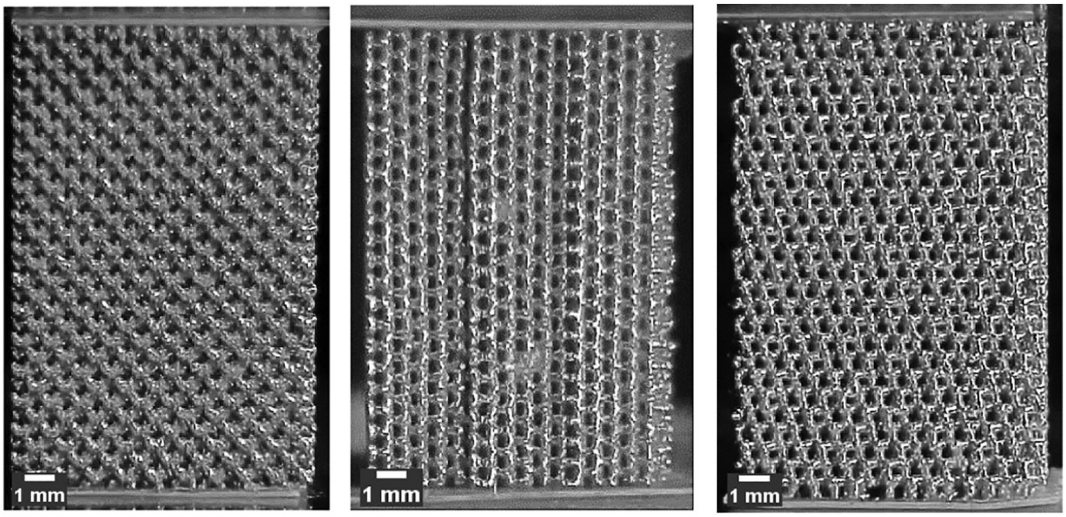

Fig. 3. Manufactured samples in (a) [001], (b) [011], (c) [111] orientations [11].

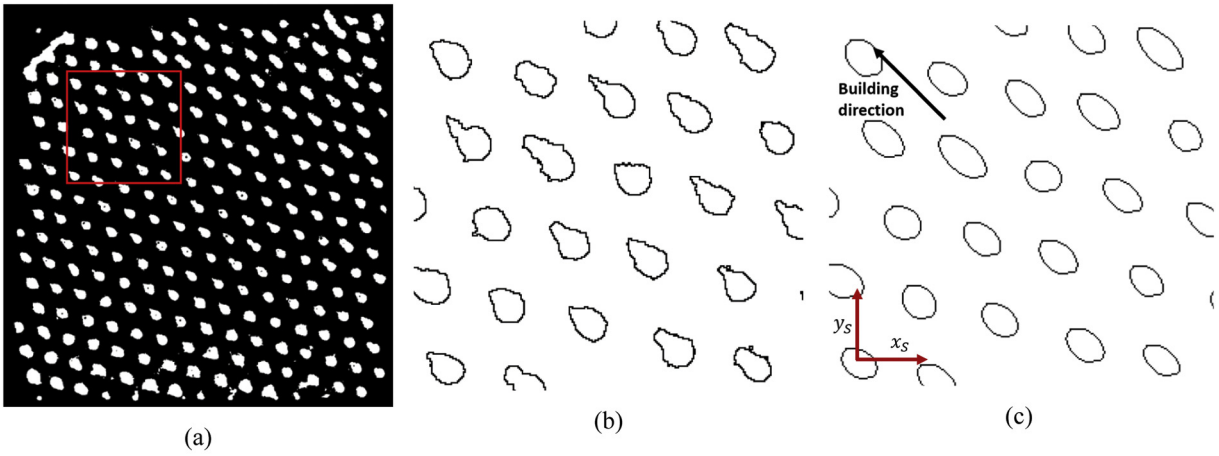

Fig. 4. (a) Stacked image from $\mu - CT$ scan, (b) detection of each cross-section, (c) best ellipse fit for every cross-section.

- all the strut cross-sections whose center of gravity reside in the defined region of interest were assigned to a single strut.

In this way, it was possible to isolate the evolution of the cross-section along the length of every strut. Three representative strut cross-sectional area distributions are presented in Fig. 5a.

Furthermore, in order to perform the statistical analysis, the isolated struts were transposed to a common reference system, as it is shown in Fig. 4-b for three representative struts. The use of this procedure allowed the analysis of the morphological evolution of more than 1000 struts along the strut axis with a robust and systematical procedure.

By using this procedure it was possible to isolate three morphological imperfection categories:

- Cross-section area: difference between the nominal cross-section and actual cross-sectional area
- Shape of the cross-section: cross-section deviation from the theoretical circular shape
- Offset from axis: distance between the center of gravity of the scanned cross-section and the axis of the designed strut

2.3. Finite Element modeling and homogenization

In order to study each type of deviation and their combined effects on the diamond UC anisotropic behavior, several finite element models were built. These models consist of beam elements generated using Abaqus 2019 (Dassault Systems). The material was modelled as linear elastic with typical AM Ti6Al4V properties: a Young's modulus of 113*GPa* and Poisson's ratio of 0.342 were considered. Each strut was modelled with 35 Timoshenko first order beam elements, to be consistent with the resolution of the $\mu - CT$ scan. From the distributions of the deviations along the struts, the mean values were used to model the deviation according to its position along the strut.

For each position along the strut axis the mean values of the imperfection distribution (i.e. variation in cross-section shape, area and offset) were extracted. These values were used to model beam elements along the strut axis. This process allowed the generation of strut FE models that reproduce the mean value trends of geometrical inaccuracy. However, the variability of the data was not considered in modeling (and thus also not in the simulations), and therefore all the lattice structure models were built using the same strut FE model.

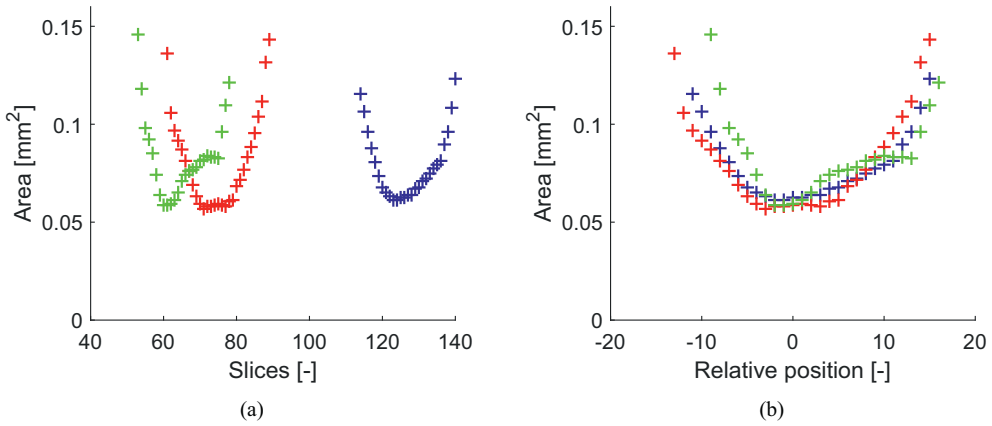

Fig. 5. (a) Absolute position of three struts (b) Relative positioning of struts along their axis.

The FE strut models were used to create 10×10×10 diamond unit cells with unit cell size of 1*mm*. Considering the type of imperfections, different models were built in order to assess both the isolated and combined effects of each type of deviation:

- Nominal: Circular and constant cross-sections, obtained as average of all mean values at each position along the strut.
- Variable Circular Cross-Section (VCCS): Circular cross-sections with variable area as measured in the $\mu - CT$.
- Constant Ellipse Cross-Section (CECS): Elliptical cross-section with constant area along the strut. The area corresponds to the average area of the ellipses.
- Constant Circular Offset Cross-Section (CCOCS): Circular and constant cross-sections as in Nominal model, in which every beam has an offset with respect to the theoretical strut axis.
- Variable Ellipse Cross-Section (VECS): Variable elliptical cross-section with values obtained from $\mu - CT$ scan.
- Variable Elliptical Offset Cross-Section (VEOCS): Elliptical cross-sections distribution as measured by the $\mu - CT$ scan, combined with the offset distribution from the strut axis. This model includes the combined effects of all measured imperfections (see Fig. 6).

The effects of the different imperfections on UC anisotropy were studied by homogenizing each FE model. This technique consists of treating each structure as if it was a homogeneous material and getting its equivalent mechanical properties. Periodic Boundary Conditions (PBC) are applied in order to analyze the behavior of the structures as if they were part of an infinite medium. In the PBC, the displacement of nodes in opposite faces of a representative volume element is constrained by relating the degrees of freedom to the mean macroscopic displacement (a detailed explanation can be found in [23]). Thus, effective elastic constants of the Eq. (1) can be obtained for each FE model according to Hooke's law for anisotropic bodies [24].

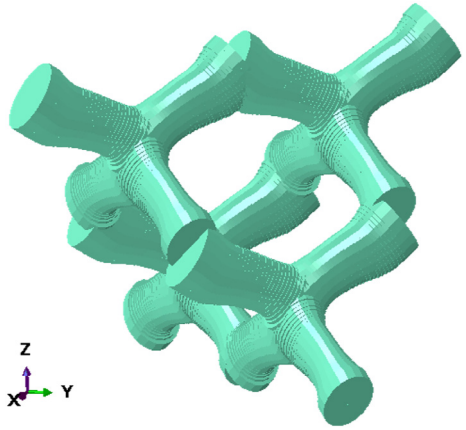

Fig. 6. VEOCS diamond unit cell model, with cross-sections scaled at 0.5.

$$\sigma = [C]\varepsilon \Rightarrow \begin{bmatrix} \sigma_1 \\ \vdots \\ \sigma_6 \end{bmatrix} = \begin{bmatrix} C_{11} & \cdots & C_{16} \\ \vdots & \ddots & \vdots \\ C_{61} & \cdots & C_{66} \end{bmatrix} \begin{bmatrix} \varepsilon_1 \\ \vdots \\ \varepsilon_6 \end{bmatrix} \tag{1}$$

A plugin developed by Omairey [23] was used to obtain the effective elastic constants of the simulated structures. This plugin applies six independent stress states, and for each case the resulting macroscopic strain tensor is obtained for the structure under PBC. As an example, for a normal macroscopic stress in direction 1, $\sigma = [\sigma_1 00000]^T$, and the resultant macroscopic strain matrix $\varepsilon = [\varepsilon_1 \varepsilon_2 \varepsilon_3 \varepsilon_4 \varepsilon_5 \varepsilon_6]^T$, the following elastic constants can be obtained for an orthotropic material:

$$E_1 = \frac{\sigma_1}{\varepsilon_1} \qquad \nu_{12} = -\frac{\varepsilon_2}{\varepsilon_1} \qquad \nu_{13} = -\frac{\varepsilon_3}{\varepsilon_1} \tag{2}$$

For shear stresses, if stress $\sigma = [00000\sigma_6]^T$ is applied, the shear modulus can be obtained as in Eq. (3), and the applied stresses and the equations are adjusted for each stress state and orientation.

$$G_{12} = \frac{\sigma_6}{\varepsilon_6} \tag{3}$$

Once the stiffness matrix [C] is obtained for each FE model it is possible to evaluate the following ratios that can be used to compare the different levels of anisotropy:

$$\text{Young's modulus ratio} = \frac{E_3}{E_1} \tag{4}$$

$$\text{Poisson's coefficient ratio} = \frac{\nu_{13}}{\nu_{12}} \tag{5}$$

$$\text{Shear modulus ratio} = \frac{G_{13}}{G_{12}} \tag{6}$$

$$\text{Anisotropy coefficient 1} = A_{23} = \frac{4C_{44}}{C_{22} + C_{33} - 2C_{23}} \tag{7}$$

$$\text{Anisotropy coefficient 2} = A_{12} = \frac{4C_{66}}{C_{11} + C_{22} - 2C_{12}} \tag{8}$$

The anisotropy coefficients are a variation of the Zener ratio. Their use allows the evaluation of non-cubic stiffness tensors. In the context

of this research, the anisotropy coefficients are used to compare levels of isotropy in different planes. Thus, in this case, coefficient values of 1 are a necessary but not sufficient condition for isotropy. For actual isotropy $C_{ii} = C_{jj}$ must also hold for $i, j = 1,2,3$.

3. Results and discussion

3.1. Metrological analysis

In a previous work, Cutolo et al. [11] defined a novel sample preparation method with particular focus on orienting the unit cell coordinate system, the sample coordinate system and the L-PBF reference system. The authors fixed the UC coordinate system parallel to the L-PBF reference system. By changing the orientation of the samples with respect to the L-PBF base plate, the authors were able to investigate the anisotropic behavior of the diamond UC. Fixing the orientation of the diamond UC with respect to the L-PBF reference system ensures that each strut axis forms the same angle of 35.26 deg with the build platform and, consequently, a high level of strut-to-strut consistency in terms of strut dimensions is guaranteed. This has been confirmed by the results of the metrological analysis performed on the $\mu - CT$ data. Therefore, it can be assumed that all the struts in each unit cell of the lattice structure exhibits the same mechanical response.

Each strut has been isolated from the reconstructed model and sectioned with 35 planes perpendicular to the strut axis. From the cross-sectional analysis, several properties were extracted regarding the morphological differences with respect to the idealized strut.

The histograms in Fig. 7 show the distributions of morphological characteristics of the struts over 3 successive slices. A representation of the location of each cross-section along an ideal strut is also given in the figures: Slice 1 corresponds to the closest slice to the node, slice 8 is about the quarter of the strut length, and slice 15 is close to the center of the strut. Fig. 7a shows the very large difference in the cross-sectional area distribution along the different sections of the strut. Apart from the changes in the mean value, the data dispersion is also very different depending on the cross-section along the strut. As a result the data distribution type is not uniform and it would not be accurate to adjust all the cross-sectional area values to a single probability distribution.

Fig. 7b shows the eccentricity distribution across three sections. The eccentricity is the normalized distance between the center and the focus of an ellipse, and is defined as follows: $ecc = \sqrt{a^2 - b^2}/a$, with a and b being the major and minor semi-axes, respectively. For a circle, the focus and the center are the same ($ecc = 0$), which is the case of the designed lattice structure. Therefore, eccentricity indicates how close an ellipse is to circularity, and can be used to assess the struts cross-section shape quality.

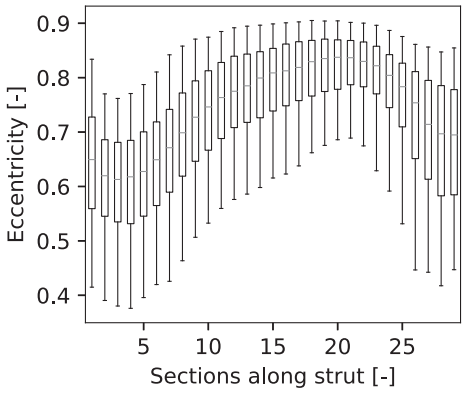

Fig. 8. Distribution of cross-section eccentricity along the strut.

Even if the cross-sectional area distributions of sections 8 and 15 are similar, Fig. 7b indicates that the eccentricity distributions have significant differences, which means that even in the regions where the area values are relatively stable, the shape of the cross-section changes.

Fig. 8 shows the evolution of the eccentricity along the strut axis. Each boxplot represents the statistical distribution of the eccentricity at the specific section, and the markers represent the 5th, 25th, 50th, 75th, and 95th percentiles. The eccentricity distributions indicate that the cross-section is not circular at any section along the strut. Furthermore, the circularity is higher close to the nodes, where the cross-sectional area deviates more from prescribed values. This means that the circularity is caused by the manufacturing deviations themselves rather than by the design.

Fig. 9 shows the probability distribution of the center of gravity offset of each cross-section. Contrary to the cross-sectional area, the offset data distribution types are quite uniform along the strut, although a clear difference in mean values can be noticed along the strut sections.

In Fig. 10 the cross-sectional area distributions are presented in terms of boxplots for each section along the strut axis. The most notable result is that the cross-sectional area decreases towards the middle of each strut indicating that less material is present in this region. On the other end, a cross-sectional area increase with a consequent mass increase can be observed approaching the two end nodes. From these data, it was possible to extract the equivalent radius distribution for each section. The VCCS strut model was generated using the mean value of the distributions presented in Fig. 10.

From the morphological analysis of the cross-section it has been noticed that the geometry of the strut cross-section deviates from the designed circular shape and tends to become elliptical. In Fig. 11 the distribution of the minor and major axis of the best fitting ellipses are

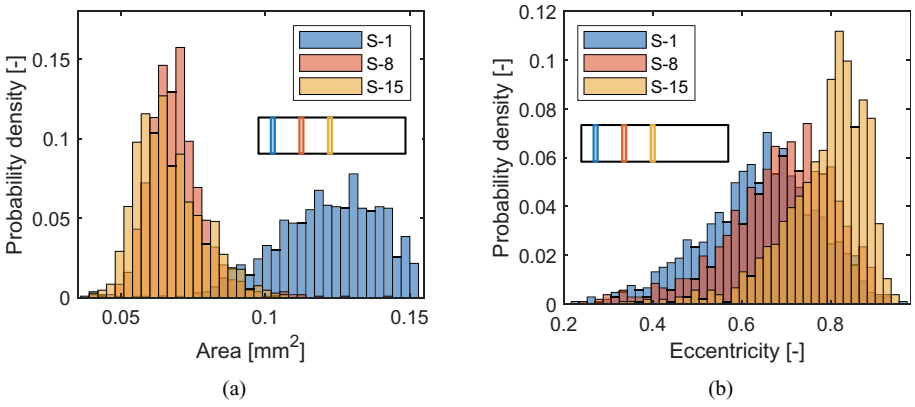

Fig. 7. Histogram of area distribution (a) and eccentricity (b) in three different sections along the strut.

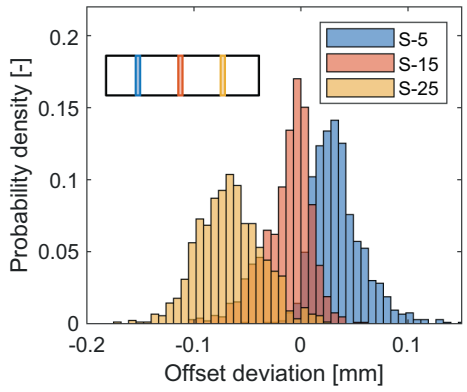

Fig. 9. Probability distribution of the offset of the center of gravity.

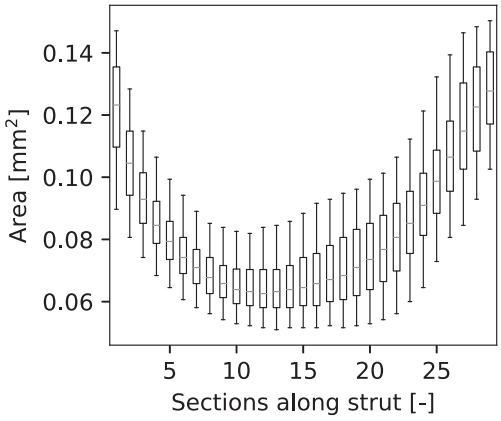

Fig. 10. Distributions of the cross-sectional area along the strut.

presented. Data are presented for each section along the strut axis in terms of boxplots. Both major and minor axes have a minimum value close to the center of the strut and higher values are reported for sections close to the nodes.

Another important feature extracted for each cross-section, was the orientation of the major and minor axis of the ellipses. From the analysis of the data it is shown that the major axis of each cross-section is oriented along the building direction. The elongated cross-section along the building direction indicates that this geometrical difference from

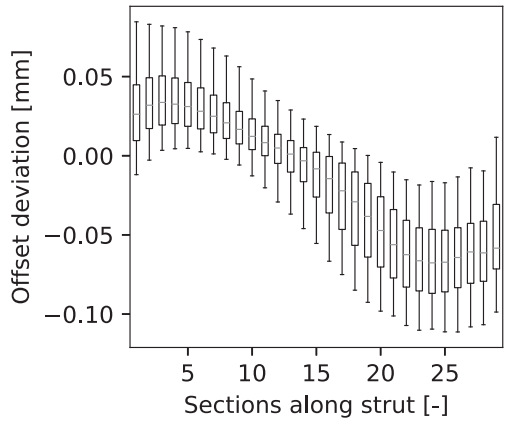

Fig. 12. Center of gravity deviation with respect the ideal strut axis.

the nominal circular shape is caused by the dross formation occurring underneath down-facing surfaces. It is also important to note that the dispersion of the data is much higher in the case of the major axis, which indicates that the dross formation is not uniform and has a high variability. The CECS FE model was created by assigning constant elliptical cross-section to the 35 Timoshenko beams for every strut. The area of the elliptical cross-section is equal to the mean value of the area distribution of Fig. 10. The VECS FE model was defined by including the information of Figs. 10 and 11 to account for the combined effect of the change in cross-section geometry and area along the strut axis.

The offset of the cross-sections follows a sort of wave distribution along the strut axis as indicated in Fig. 12. The center of gravities are shown for each section, and the 0 offset is assumed as the mean of 10 slices along the strut with lowest cross-sectional area. These cross-sections are less affected by the dross formation, and therefore their center of gravity is closer to the design values. For each strut the center of gravity offset results positive for the node that is closer to the built platform, decreasing along the strut longitudinal axis. This produces a lower strut inclination, leading to an angle between the horizontal plane and the axis of the strut smaller than 35.26 deg.

Fig. 13 shows the centers of gravity of each strut element projected on the plane perpendicular to the strut axis. It is interesting to notice that the drift of the center of gravity lies along a direction that is parallel to the building direction. With this information the CCOCS FE model was created consisting of 35 beam elements per strut, with circular cross-section. The centers of gravity were drifted following the distribution

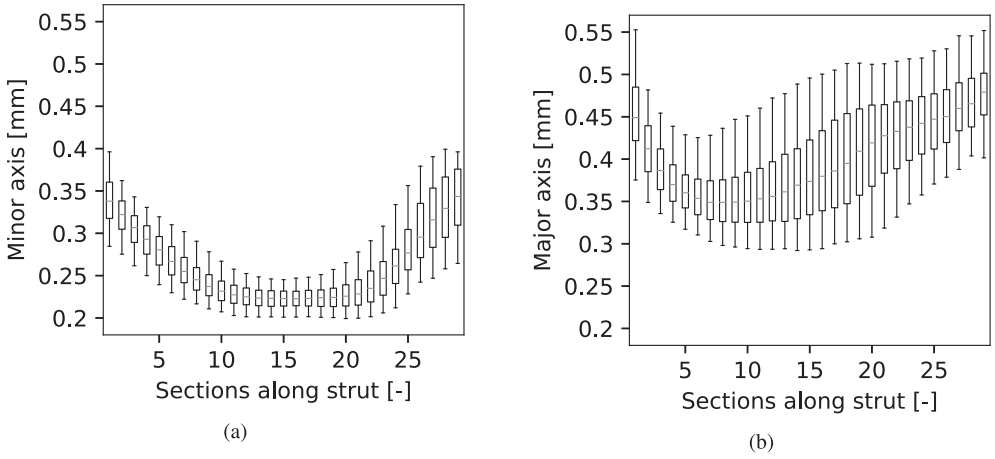

Fig. 11. Distribution of the (a) minor axis and (b) major axis of the elliptical cross-section along the strut axis.

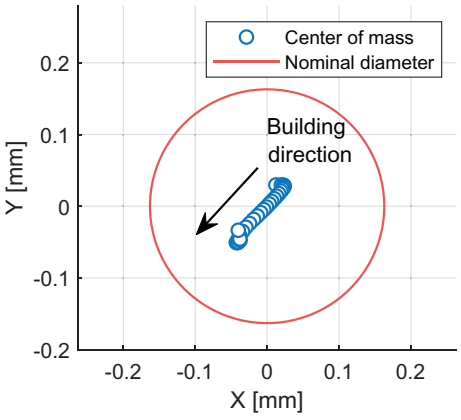

Fig. 13. Offset of the strut center of gravity along the length of the strut.

of mean values shown in Fig. 12. Combining the information of Figs. 10-12 the VEOCS FE model was generated.

3.2. FE results

The VCCS, CECS and CCOCS strut models were used to generate FE models of the diamond based lattice structure to evaluate the impact of a single geometrical imperfection on the anisotropic behavior of the diamond unit cell. The VECS and VEOCS strut models were used to evaluate the combined effect of the geometrical deviations on the anisotropic behavior of the diamond UC.

The homogenization process was performed on all the FE models generated to evaluate their directional stiffness and anisotropic coefficients from Eq. (2). Results of this analysis for different directions (i.e. [100], [001], [110], [011] and [111]) are reported in Fig. 14. Moreover, in order to visually express the impact of the different imperfections on the anisotropic behavior of the diamond unit cell, the homogenized Young's moduli were also plotted as 3 dimensional surfaces. These representations were used to clearly identify the strong and weak directions.

Fig. 15b plots the homogenized Young's modulus of the Nominal FE model showing the elastic anisotropy of the ideal diamond unit cell. The 3D surface plot clearly indicates a cubic anisotropic behavior, with shear directions (i.e.[111] directions) presenting the higher value of the Young's modulus and the orthonormal directions (i.e. [100], [010] and [001]) resulting the weaker directions. The principal planes XY and YZ present the same anisotropy. The high level of anisotropy is also indicated by the anisotropy coefficients A_{23} and A_{12}.

These results have been used as reference case and compared with the outcomes of the homogenization process performed on the other FE models. The comparisons have been made by means of polar plots obtained as indicated in Fig. 16: (i) the xy polar plot has been obtained intersecting the 3D directional stiffness surfaces with an ideal XY plane; (ii) the YZ polar plot has been obtained intersecting the 3D directional stiffness surfaces with an ideal YZ plane; (iii) the Ï€ polar plot obtained by intersecting the 3D directional stiffness surfaces with the plane formed by [111] and [110] directions.

3.3. Effect of change of cross-sectional area

The change of the cross-sectional area along the strut axis (Fig. 10) was used to generate the VCCS lattice structure. The homogenized Young's modulus surface presents a similar anisotropic behavior compared to the Nominal model. The polar plots shown in the first row of Table 1 indicate cubic anisotropy with equal stiffness in orthonormal directions and in shear directions. Comparing VCCS and Nominal results it can be noticed that VCCS presents higher stiffness along all the directions. The reason for this can be attributed to the fact that the nodes have bigger cross-section. As indicated by Van Hooreweder et al. [25], the maximum tensile and compressive stresses develop in regions close to the nodes of the struts. Higher dimensions of the cross-section in the nodal regions generate lower value of the nodal tensile and compressive stresses. Therefore, the distribution of the cross-section area along strut axis (Fig. 10) has a beneficial impact on the overall stiffness of the structure. Variation of the cross-sectional area also has an impact on the anisotropy of the diamond UC. As indicated in Fig. 13, the Young's, Poisson's and Shear ratios remain constant while A_{23} and A_{12} are reduced indicating a lower degree of anisotropy.

3.4. Effect of the constant elliptical cross-section

The homogenized Young's modulus surface of the CECS presents some difference with respect to the Nominal. The CECS doesn't present cubic anisotropy as the Nominal model. In fact, along the orthonormal directions different values of the Young's modulus are reported with [001] being stiffer than [100] direction as shown in Fig. 14a. The polar plots of the second row of Table 1 show that CECS possesses a lower stiffness and a lower anisotropy level across the YZ plane. This behavior is confirmed by the decrease of A_{23} coefficient and the increase of A_{12}.

The Poisson's and the shear ratios shown in Fig. 14b are systematically lower than the Nominal ones highlighting a shear stiffness transfer from YZ plane to XY plane.

These stiffness changes are the result of the change in cross-sectional shape. In fact the orientation of the major axis of the ellipse plays an

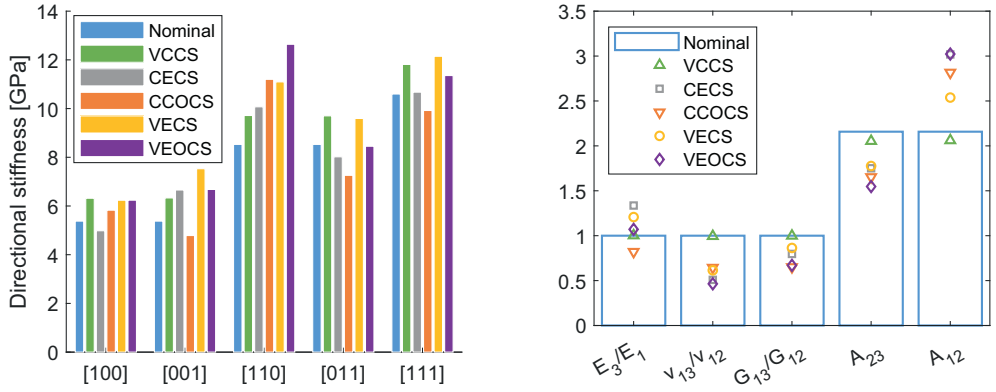

Fig. 14. (a) Directional stiffness along a particular direction (b) Anisotropic coefficients.

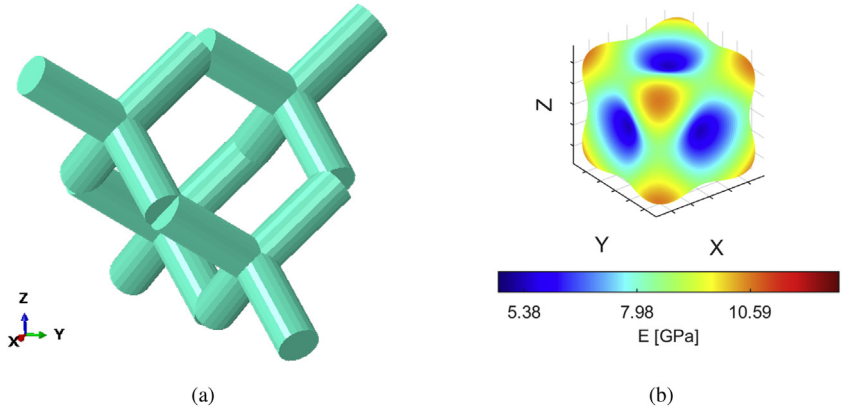

Fig. 15. (a) Unit cell of Nominal FE model and (b) its directional stiffness.

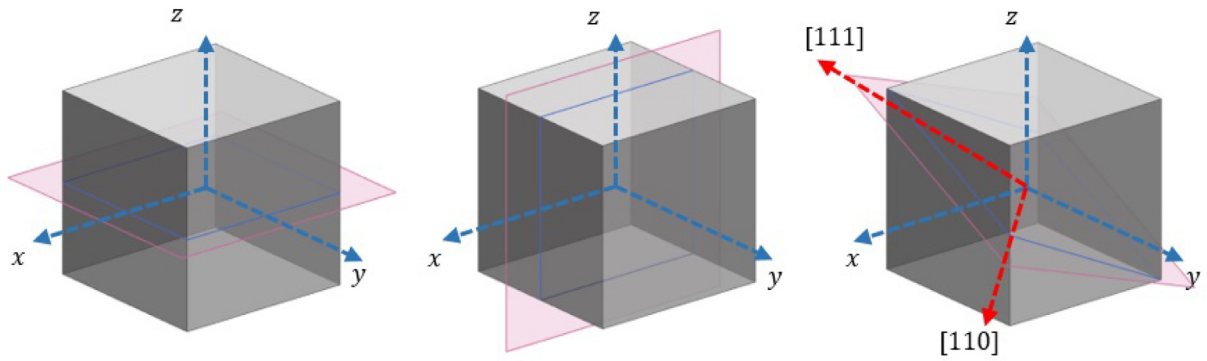

Fig. 16. Plane identification for (a) *XY* polar plot, (b) *XZ* polar plot, (c) π polar plot.

important role to explain this behavior. When the major axis is parallel to the load direction the structure is able to better absorb the external loads due to the higher inertia of the cross-section around the minor axis. On the contrary, if the load direction has the same orientation of the minor axis, the lower inertia makes the structure weaker.

3.5. Effect of the offset of the cross-section

The change in the position of the cross-section's centers of gravitiy has a significant impact on the mechanical properties of the lattice structure. The CCOCS directional stiffness of Fig. 13 and the polar plots of the third row in Table 1 indicate that this model does not present cubic anisotropy. The orthonormal directions perform differently with [001] direction being weaker than [100]. Moreover, the stiffer direction changes from the shear [111] direction to [110]. More information regarding the anisotropic characteristics of the CCOCS model can be extracted from Fig. 14. First of all, the decrease of A_{23} suggests higher isotropy on XZ and YZ planes whilst the increase of A_{12} indicates a higher level of anisotropy on XY plane. Secondly, ν_{13}/ν_{12} and G_{13}/G_{12} ratios suggest a stiffness transfer from plane YZ and XZ to XY plane.

The stiffness surface distribution of CCOCS differences with the nominal model can be attributed to the reduced inclination of the struts axis with respect to the building direction resulting from the wave distribution of the cross-sections offsets. According to the local stress method developed by Van Hooreweder et al. [25] for bending dominated diamond unit cells, the angle between the horizontal plane and the strut axis determine the stress distribution across the node. For diamond unit cells this angle is equal to 35.26 deg. A reduction of this angle causes a change of the distribution of the total load in axial and bending components. The axial load is a more efficient way to carry the loads, thus, the directions which maximize this component have a higher stiffness and lower bending stresses. The opposite happens for directions with a higher bending load component with respect to the nominal.

3.6. Combined effects: elliptical variable cross-section

The homogenized Young's modulus for the VECS model are shown in the fourth row of Table 1. The polar plots follow the same trend as the CECS indicating that the effect of the change in cross-section geometry largely impact the mechanical behavior of the diamond lattice structure. On the other hand, a general increase of the stiffness in all the direction can be observed. This is the result from the variability of the cross-sectional area.

The combined effect of the variable elliptical cross-section is also affecting the anisotropy coefficient expressed by Eq. (2). The anisotropy level across XZ and YZ planes decreases with respect to the nominal model as well as for the CECS model. On the contrary, the anisotropy level across XY plane increases but not as much as for the CECS model. This attenuation is due to the different stress distribution along the strut axis generated by the variation of cross-sectional area.

3.7. Combined effects: offset elliptical variable cross-section

The VEOCS homogenized stiffness presents the combined effect of the three different deviation typologies as shown in the last row of Table 1. The maximum directional stiffness is expressed by [110] directions and the weakest direction being [100] as effect of the offset of the cross-sections. The orthonormal stiffness are enhanced because of the effect of the change in cross-sectional area distribution. If compared with the nominal model, the VEOCS anisotropic behavior results

Table 1
Comparisons of VCCS, CECS, VECS, CCOCS and VEOCS directional stiffness with the Nominal.

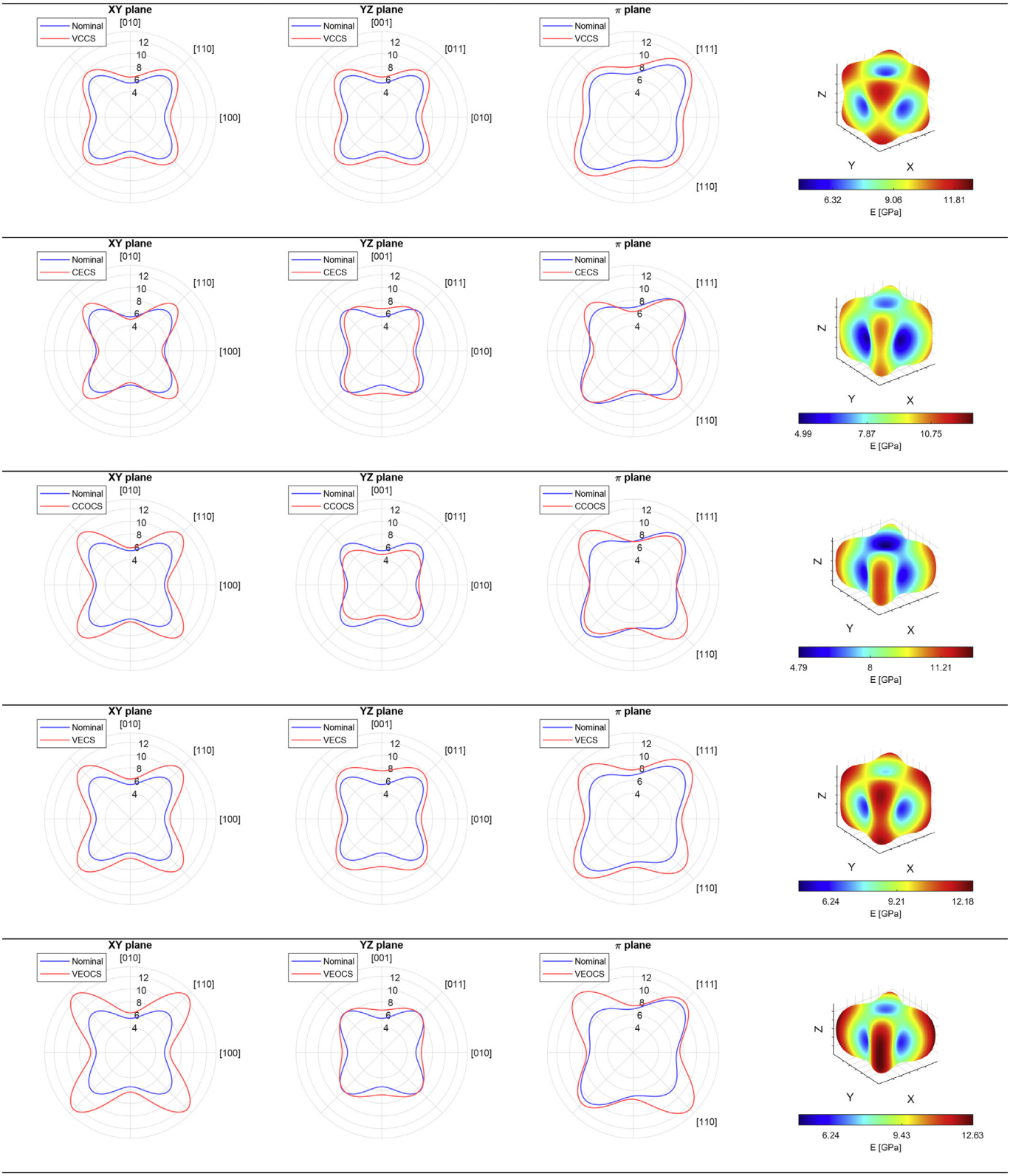

different: the YZ polar plot shows a very low degree of anisotropy, confirmed by the low value of A_{23}; on the other hand, XY and Ï€ polar plots indicate a very high anisotropic behavior. These two combined effects are the result of the lower struts inclination with respect to the horizontal plane superimposed to the change of the cross-sectional geometry.

3.8. Comparison with experimental results

Table 2 shows the homogenized stiffness evaluated for all the different FE models. Considering that the as-produced samples suffer from the three types of morphological imperfection, i.e. variation of cross-

Table 2
Comparison of the directional stiffness as predicted by different FE strategies.

	100	001	110	011	111
	(GPa)	(GPa)	(GPa)	(GPa)	(GPa)
Nominal	5,38	5,38	8,53	8,53	10,60
VCCS	6,32	6,33	9,72	9,70	11,81
CECS	4,98	6,66	10,07	8,02	10,67
CCOCS	5,83	4,79	11,20	7,26	9,92
VECS	6,24	7,53	11,10	9,59	12,15
VEOCS	6,24	6,68	12,64	8,45	11,36

sectional area, geometry and center of gravity, the FE model that better replicates the anisotropic behavior of the lattice structures is the VEOCS. In fact, the stiffest direction of the VCOCS structure changes from [111] in the ideal case to [110]. This result is in line with the experimental results presented in [8] in which [110] oriented structure was reported to have the highest stiffness.

This behavior is related to the combined effect of the center of gravity offsets and change in cross-sectional shape. These types of imperfections are mainly developed during the manufacturing process of the lattice structure due to dross formation underneath unsupported struts. As a matter of fact, during the L-PBF production of inclined struts, the laser tends to melt more powder than needed, elongating the strut cross-sectional shape along the build direction. Struts with small diameters and high diameter/length ratios, as the ones produced by Cutolo et al., are more affected by this phenomena. The change in cross-sectional shape produces also a change of the cross-section center of gravity with respect to the ideal case.

This phenomenon is not exclusive for Ti6Al4V nor for the diamond unit cell, and it can affect any lattice structure manufactured by L-PBF. Therefore, qualitatively similar effects are expected for other materials and unit cells, which are still to be studied. The procedure explained in this work can be used for other cases to assess the manufacturing deviations and predict their effect in the anisotropy by combining $\mu - CT$ data and FE simulations.

There are different approaches to overcome the morphological imperfections of these lattice structures: manufacturing parameters can be changed to try to reduce the dross formation in down-facing zones. On the other hand, the circularity of the cross-section can be improved by designing elliptical struts with reversed major and minor axes, in order to compensate the dross formation in manufacturing. Similarly, the cross-sectional area close to the nodes could be reduced in the design phase.

Finally, since these imperfections are more prevalent in small strut diameters, and with high diameter/length ratios, increasing the unit cell size while maintaining the relative density can be an option to obtain a lattice structure with equivalent mechanical properties and smaller deviations. Nonetheless, there are applications that require very small pore sizes, such as in the biomedical field. In this case, increasing unit cell size is not an option, and therefore, understanding the anisotropy of the lattice structures with small unit cell size and manufacturing deviations is of great importance.

4. Conclusions

Manufacturing imperfections have a significant impact on the anisotropy of lattice structures produced by L-PBF, and their effect is not limited to a uniform decrease of the stiffness and strength. These deviations change the elastic response of the lattice structure in a variable way depending on the load direction, and each of the studied imperfection types have a specific impact on the directional stiffness of the lattice structure.

The variation of the cross-sectional area increases the efficiency of the load carrying capacity for bending dominated lattice structures in any direction. This is caused by a higher bending load close to the nodes compared to the central part of the strut. On the other hand, the elliptical cross-section and the offset of the center of gravity have very direction dependent effects. The elliptical cross-section is especially significant in bending dominated lattice structures, since the directional stiffness change is driven by the higher inertia of the major axis compared to the minor axis. Regarding the offset of the center of gravity, the trend of the deviation is uniform enough to consider it as a change of the orientation of the strut axis and reduction of its angle with respect to the building plane. This varies the proportion of axial and bending load compared to the nominal structure. Thus, the anisotropy is affected because of the difference between the axial and bending stiffness of the beam.

Very clear trends can be observed on every deviation type depending on their proximity to the nodes. Therefore, it is necessary to take into account the position of the manufacturing deviations along the strut in order to explain their effect in the anisotropy. Moreover, these imperfections are highly dependent on the diameter to length ratio, unit cell size and relative density, as well as manufacturing parameters, and the observed trends are more significant when working closer to manufacturability limits.

The offset of the center of gravity has the most remarkable impact on the anisotropy because it changes the stiffest direction from [111] to [110], which can also be observed in experimental data. This has major implications when using this type of lattice structures in load bearing applications in which the structure needs to be oriented so as to minimize compliance.

Data availability

The raw and processed data required to reproduce these findings are available to download from: https://doi.org/10.5281/zenodo.3862128.

Declaration of Competing Interest

The authors declare that they have no known competing financial interests or personal relationships that could have appeared to influence the work reported in this paper.

Acknowledgement

The authors are grateful for the financial support for international movility of Fundación Bancaria “La Caixa” and to the “Interne Fondsen KU Leuven/Internal Funds KU Leuven”.

References

[1] J. Kruth, P. Mercelis, J. Van Vaerenbergh, L. Froyen, M. Rombouts, Binding mechanisms in selective laser sintering and selective laser melting, Rapid Prototyp. J. 11 (1) (2005) 26–36, https://doi.org/10.1108/13552540510573365.

[2] T. Maconachie, M. Leary, B. Lozanovski, X. Zhang, M. Qian, O. Faruque, M. Brandt, SLM lattice structures: properties, performance, applications and challenges, Mater. Des. 183 (2019) 108137, https://doi.org/10.1016/j.matdes.2019.108137.

[3] B. Nagesha, V. Dhinakaran, M.V. Shree, K.M. Kumar, D. Chalawadi, T. Sathish, Review on characterization and impacts of the lattice structure in additive manufacturing, Materials Today: Proceedings international Conference on Recent Trends in Nanomaterials for Energy, Environmental and Engineering Applications, 21, 2020, pp. 916–919, https://doi.org/10.1016/j.matpr.2019.08.158http://www.sciencedirect.com/science/article/pii/S2214785319331451.

[4] V. Papetti, P.D. Eggenschwiler, A.D. Torre, F. Lucci, A. Ortona, G. Montenegro, Additive manufactured open cell polyhedral structures as substrates for automotive catalysts, Int. J. Heat Mass Transf. 126 (2018) 1035–1047, https://doi.org/10.1016/j.ijheatmasstransfer.2018.06.061http://www.sciencedirect.com/science/article/pii/S0017931017355515.

[5] M. Ashby, The properties of foams and lattices, Philos. Trans. R. Soc. A Math. Phys. Eng. Sci. 364 (1838) (2006) 15–30, https://doi.org/10.1098/rsta.2005.1678.

[6] M.F. Ashby, Hybrids to fill holes in material property space, Philos. Mag. 85 (26) (2005) 3235–3257, https://doi.org/10.1080/14786430500079892.

[7] L. Gibson, M. Ashby, Cellular Solids: Structure and Properties, Pergamon Press, 1988.

[8] J. C. M. F.R.S, L. on the calculation of the equilibrium and stiffness of frames, Lond. Edinb. Dublin Philos. Mag. J. Sci. 27 (182) (1864) 294–299. doi:https://doi.org/10.1080/14786446408643668.

[9] R. Wauthle, B. Vrancken, B. Beynaerts, K. Jorissen, J. Schrooten, J.-P. Kruth, J. Van Humbeeck, Effects of build orientation and heat treatment on the microstructure and mechanical properties of selective laser melted ti6al4v lattice structures, Addit. Manuf. 5 (2015) 77–84, https://doi.org/10.1016/j.addma.2014.12.008http://linkinghub.elsevier.com/retrieve/pii/S2214860414000323.

[10] H. Soul, P. Terriault, V. Brailovski, The static and fatigue behavior of AlSiMg alloy plain, notched, and diamond lattice specimens fabricated by laser powder bed fusion, J. Manuf. Mater. Process. 2 (2) (2018) 25, https://doi.org/10.3390/jmmp2020025http://www.mdpi.com/2504-4494/2/2/25.

[11] A. Cutolo, B. Engelen, W. Desmet, B. Van Hooreweder, Mechanical properties of diamond lattice ti6al4v structures produced by laser powder bed fusion: on the effect of the load direction, J. Mech. Behav. Biomed. Mater. 104 (2020) 103656, https://doi.org/10.1016/j.jmbbm.2020.103656http://www.sciencedirect.com/science/article/pii/S1751616119314353.

[12] K. Lietaert, A. Cutolo, D. Boey, B. Van Hooreweder, Fatigue life of additively manufactured Ti6Al4V scaffolds under tension-tension, tension-compression and compression-compression fatigue load, Sci. Rep. 8 (2018) 4957, https://doi.org/10.1038/s41598-018-23414-2https://www.nature.com/articles/s41598-018-23414-2.

[13] L. Yang, C. Yan, H. Fan, Z. Li, C. Cai, P. Chen, Y. Shi, S. Yang, Investigation on the orientation dependence of elastic response in gyroid cellular structures, J. Mech. Behav. Biomed. Mater. 90 (2019) 73–85, https://doi.org/10.1016/j.jmbbm.2018.09.042http://www.sciencedirect.com/science/article/pii/S1751616118308506.

[14] S. Van Bael, G. Kerckhofs, M. Moesen, G. Pyka, J. Schrooten, J.P. Kruth, Micro-CT-based improvement of geometrical and mechanical controllability of selective laser melted ti6al4v porous structures, Mater. Sci. Eng. A 528 (24) (2011) 7423–7431, https://doi.org/10.1016/j.msea.2011.06.045http://www.sciencedirect.com/science/article/pii/S092150931100712X.

[15] H. Hassanin, Y. Alkendi, M. Elsayed, K. Essa, Y. Zweiri, Controlling the properties of additively manufactured cellular structures using machine learning approaches, Adv. Eng. Mater. 22 (3) (2020) 1901338 , arXiv:https://onlinelibrary.wiley.com/doi/pdf/10.1002/adem.201901338 https://doi.org/10.1002/adem.201901338https://onlinelibrary.wiley.com/doi/abs/10.1002/adem.201901338.

[16] C. Qiu, S. Yue, N.J. Adkins, M. Ward, H. Hassanin, P.D. Lee, P.J. Withers, M.M. Attallah, Influence of processing conditions on strut structure and compressive properties of cellular lattice structures fabricated by selective laser melting, Mater. Sci. Eng. A 628 (2015) 188–197, https://doi.org/10.1016/j.msea.2015.01.031http://www.sciencedirect.com/science/article/pii/S0921509315000453.

[17] C. Tan, S. Li, K. Essa, P. Jamshidi, K. Zhou, W. Ma, M.M. Attallah, Laser powder bed fusion of ti-rich tini lattice structures: Process optimisation, geometrical integrity, and phase transformations, Int. J. Mach. Tools Manuf. 141 (2019) 19–29, https://doi.org/10.1016/j.ijmachtools.2019.04.002http://www.sciencedirect.com/science/article/pii/S0890695519300392.

[18] M. Dallago, B. Winiarski, F. Zanini, S. Carmignato, M. Benedetti, On the effect of geometrical imperfections and defects on the fatigue strength of cellular lattice structures additively manufactured via selective laser melting, Int. J. Fatigue 124 (2019) 348–360, https://doi.org/10.1016/j.ijfatigue.2019.03.019http://www.sciencedirect.com/science/article/pii/S0142112319300957.

[19] H. Lei, C. Li, J. Meng, H. Zhou, Y. Liu, X. Zhang, P. Wang, D. Fang, Evaluation of compressive properties of SLM-fabricated multi-layer lattice structures by experimental test and Î¼-CT-based finite element analysis, Mater. Des. 169 (2019) 107685, https://doi.org/10.1016/j.matdes.2019.107685http://www.sciencedirect.com/science/article/pii/S0264127519301224.

[20] B. Lozanovski, M. Leary, P. Tran, D. Shidid, M. Qian, P. Choong, M. Brandt, Computational modelling of strut defects in SLM manufactured lattice structures, Mater. Des. 171 (2019) 107671, https://doi.org/10.1016/j.matdes.2019.107671http://www.sciencedirect.com/science/article/pii/S026412751930108X.

[21] L. Liu, P. Kamm, F. GarcÃ-A-Moreno, J. Banhart, D. Pasini, Elastic and failure response of imperfect three-dimensional metallic lattices: the role of geometric defects induced by selective laser melting, J. Mech. Phys. Solids 107 (2017) 160–184, https://doi.org/10.1016/j.jmps.2017.07.003http://www.sciencedirect.com/science/article/pii/S0022509616307608.

[22] L. Xiao, S. Li, W. Song, X. Xu, S. Gao, Process-induced geometric defect sensitivity of ti6al4v lattice structures with different mesoscopic topologies fabricated by electron beam melting, Mater. Sci. Eng. A 778 (2020) 139092, https://doi.org/10.1016/j.msea.2020.139092http://www.sciencedirect.com/science/article/pii/S0921509320301805.

[23] S.L. Omairey, P.D. Dunning, S. Sriramula, Development of an ABAQUS plugin tool for periodic RVE homogenisation, Eng. Comput. 35 (2) (2019) 567–577, https://doi.org/10.1007/s00366-018-0616-4.

[24] P. Vannucci, General Anisotropic Elasticity, 85, Springer Singapore, 2018 19–73, https://doi.org/10.1007/978-981-10-5439-6http://link.springer.com/10.1007/978-981-10-5439-6.

[25] B. Van Hooreweder, Y. Apers, K. Lietaert, J.-P. Kruth, Improving the fatigue performance of porous metallic biomaterials produced by selective laser melting, Acta Biomater. 47 (2017) 193–202, https://doi.org/10.1016/j.actbio.2016.10.005http://www.sciencedirect.com/science/article/pii/S1742706116305232.